Three-dimensional stochastic modeling of metallic surface roughness resulting from pure waterjet peening

J.Xie[a,*], D.Rittel[a]

[a]*Faculty of Mechanical Engineering, Technion - Israel Institute of Technology, 32000 Haifa, Israel*

Abstract

We propose a new approach named FEM-Stochastic approach for predicting the surface roughness resulting from waterjet peening of a metallic surface. This approach consists three aspects. One is Coupled Eulerian Lagrangian (CEL) simulation for studying the deformation behavior of single droplet; the second is the stochastic analysis for synthesizing a deformed surface; the third is to calculate the surface roughness parameters. CEL simulation results agree well with the liquid impact theory. Four situations with a different number of droplets (1000, 5000, 10000 and 20000) are analyzed, for which the deformed target surfaces and corresponding roughness profiles are shown and compared. Calculated values of roughness parameters indicate that there are three stages of evolution for the arithmetic average height R_a and quadrature average R_q. Those are: roughness increase stage, roughness decrease and roughness steady-state stage, respectively. The total roughness R_t and kurtosis parameter R_{ku} decline gradually when more and more droplets are modeled because the sharp ridges formed by fewer droplets are obliterated by the impingement of subsequent droplets. Skewness parameter R_{sk} values are all negative, no matter how many droplets, moreover, its absolute value becomes increasingly smaller as the number of droplet changes from 1000 to 20000. The present spatial model of droplets, although still incomplete, is capable of synthesizing a deformed surface and calculating the relevant roughness parameters.

Keywords: Waterjet Peening, Surface Roughness, Finite element modeling,

*Corresponding author

Email address: jingxie@technion.ac.il (J.Xie)

1. Introduction

We showed in a previous paper that a two dimensional analysis cannot determine the surface roughness profile of a waterjet peened metallic surface (Xie and Rittel, 2017). The problem will therefore be tackled from another perspective. For this, one needs to reconsider the peening process, particularly the contact between waterjet and target material surface, with the involvement of a very large number of single droplet impacts. In region II of the jet, the water column has transformed into a myriad of droplets with different diameters due to the atomization effect. The impact pressure is an accumulative consequence of every droplet impact. It is neither continuous along the axial direction nor is it smooth along the radial direction.

In this paper, we propose a new approach, as illustrated in Fig. 1, which consists of modeling the single droplet impact at first, then devising a method to add/average all the individual contributions in order to reproduce the deformed surface, and finally calculating the resulting roughness parameters based on that synthetic surface profile.

Many papers regarding droplet dynamics have been published since the 19^{th} century. The English physicist A.M.Worthington gave a fascinating introduction to this field in 1876 (Worthington, 1876), and his book "*A Study of Splashes*" concludes all his main research achievements on the physics of splashes. Yarin published a review article (Yarin, 2006) which surveys the drop impact dynamics from experimental, theoretical and computational aspects. Likewise, experimental work due to Rioboo et al. (Rioboo et al., 2001) revealed six possible morphology of drop impact on a dry surface.

As of today, finite element packages, such as Abaqus/Explicit (Abaqus, 2014), provide three available strategies for modeling the fluid-solid interaction problem: Arbitrary Lagrangian Eulerian (ALE), Smoothed Particle Hydrodynamics (SPH) and Coupled Eulerian Lagrangian (CEL). Each of them has been adopted by researchers to study the waterjet machining problem.

Mabrouki (Mabrouki et al., 2000), Maniadaki (Maniadaki et al., 2007) and Gong (Wenjun et al., 2011) used ALE implemented in LS-DYNA 3D code to handle the waterjet and target interaction problem. Ma (Ma et al., 2008) compared three computational models and stated the SPH-FEM hybrid model they developed was more efficient than ALE when dealing with

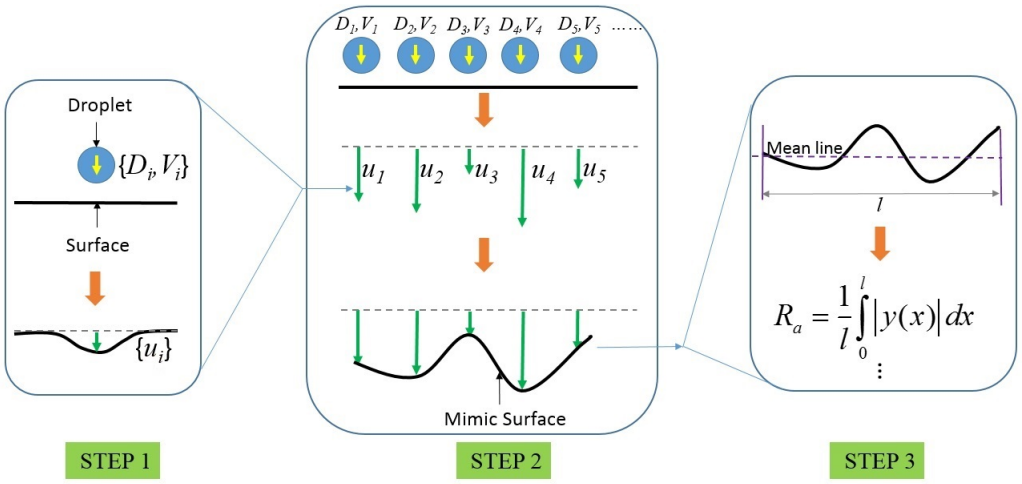

Figure 1: Schematic representation of the FEM - Stochastic analysis procedures. STEP 1: model the single droplet impact and obtain the maximum vertical displacement of target surface; STEP 2: place a large number of droplets into the contact area and assume each droplet produces a vertical deformation according to the results of STEP 1 and connect all the endpoints of deformation vectors to synthesize a surface; STEP 3: calculate the various surface roughness parameters.

the fluid-solid interaction, especially the waterjet penetration problem. Hsu (Hsu et al., 2013) used CEL technique to simulate a waterjet at a speed of 570 m/s impacts on a flat PMMA plate, and provided an accurate quantitative details of stress, strain and deformation fields that would be difficult to reproduce experimentally. At the time of droplet collapse, the droplet undergoes a large amount of volumetric deformation at a high strain rate. Based on our previous experience (Xie et al., 2015), the CEL is a good choice for eliminating the element distortion problem which frequently occurs during the simulation process of high strain rate and high strain gradient problem.

Specification of droplet size in the downstream of waterjet is not only of utmost importance for the design, operation, and optimization of waterjet systems, but also for our prediction. Experimental results showed that the droplet ranges from infinitesimal to a maximum of 200 μm (Sellens, 1989; Boyaval and Dumouchel, 2001). A finite maximum diameter exists because aerodynamic forces and a non-zero minimum diameter exists because of the cohesive surface tension forces. Since small droplets do not have enough momentum to travel a long distance, a gradation of droplet sizes in the waterjet axial direction occurs, and thus only large droplets exist in the

downstream locations (Yoon et al., 2004). The same phenomenon appears along the radial direction (Li et al., 1991). Large droplets are less affected by the air entrainment and subsequent interact with turbulent eddies in the entrained air, while smaller droplets are generally swept toward the waterjet centerline. Eventually all the droplets will have more uniform size at farther downstream.

Babinsky and Sojka (Babinsky and Sojka, 2002) reviewed three available methods for modeling drop size distributions: the empirical method, the discrete probability function method, and the maximum entropy principle method.

The classical empirical method consists of collecting data for a wide range of nozzles and operating conditions then fitting the data to a curve. A few popular empirical distributions used are log - normal, root - normal, Rosin - Ramble, Nukiyama - Tanasawa, and log - hyperbolic distributions (Asadollahzadeh et al., 2017a,b). One can see two problems with the empirical method: first, none of the above distribution is universal and can accurately fit a large fraction of the available data; second, extrapolating the data to operating regimes beyond the experimental range is difficult.

The discrete probability function (DPF) method assumes that the initial fluid structure separates into ligaments, and these ligaments break up into ligament fragments, and finally collapse into droplets. It involves a detailed instability analysis for describing the breakup mechanism. Shinjo and Umemura (Shinjo and Umemura, 2010) captured the ligament and droplet formation by direct numerical simulation with sufficient grid resolution; however, this approach is expensive (5760 cores for 410 h).

The maximum entropy principle (MEP) method treats atomization process as a 'black box' that transforms the waterjet into a system of droplets with a particular size distribution, without detailing what happened inside the box (Dumouchel, 2009). Actually, this black box could produce an infinite number of possible size distribution, the MEP states that the most likely size distribution is the one that maximizes the entropy of the system, subject to certain constraints (Sellens and Brzustowski, 1986). The MEP method could provide the joint size-velocity distributions (Sellens, 2016; Li et al., 1990; Li and Tankin, 1992), the utility of MEP, however, requires at least two representative diameters (number/mass mean diameter, Sauter mean diameter (Azzopardi, 2011)) which must be obtained from experimental results at present, that sets a serious constraint.

As an alternative, in this work we divide the droplets into several classes,

according to their diameters and velocities. It is assumed that all droplets belonging to a given class have the same diameter/velocity equal to the median diameter/velocity of the class. All the characteristic cases determined by the median diameter and velocity are simulated and their results construct the basis data points for synthesizing the surface.

Five roughness parameters can describe the surface roughness, and their mathematical expressions (Taro et al., 2015) are as follows.

- The arithmetic average height along a sampling length l:

$$R_a = \frac{1}{l}\int_0^1 |y(x)|dx \tag{1}$$

- The total roughness is the vertical distance between the highest peak R_p and the lowest valley R_v:

$$R_t = R_p + R_v \tag{2}$$

- The quadrature average:

$$R_q = \sqrt{\frac{1}{l}\int_0^1 y^2(x)dx} \tag{3}$$

- The skewness parameter:

$$R_{sk} = \frac{1}{R_q^3}\frac{1}{l}\int_0^1 y^3(x)dx \tag{4}$$

- The kurtosis parameter:

$$R_{ku} = \frac{1}{R_q^4}\frac{1}{l}\int_0^1 y^4(x)dx \tag{5}$$

Among them, except for the skewness parameter, the others are always positive. Positive skewness means sharp peaks and round valleys, and negative skewness means round peaks and sharp valleys.

In section 2 of this paper, computational details are described including the category of droplets, CEL modelling technique and the hybrid framework

about how to combine CEL simulation and stochastic analysis. Simulation results of single droplet are given at first in section 3; consequently, a systematic analysis is conducted from 3D synthesized surfaces to 2D surface roughness profiles to the calculated values of surface roughness parameters. Validation of CEL analysis, and the influence of class width and spatial distribution of droplets on successful prediction are discussed in section 4.

2. Computational details

2.1. Class series of size and velocity

Every droplet is assumed spherical and therefore fully characterized by a diameter D_d. Since waterjet peening has a higher average inlet pressure (140-420 MPa) comparing to those experimental initial condition (0.2-15 MPa) (Sellens, 1989; Boyaval and Dumouchel, 2001; Yoon et al., 2004; Li et al., 1991), resulting in a higher kinetic energy of waterjet, which allows the large droplets (200 μm) to further breakup into smaller droplets after the primary breakup. Hence, 10 classes of diameter are defined which from 10 to 100 μm with an equal interval of 10 microns.

Larger droplets ($D_d > 100\mu m$) exist, but with a very small probability (Boyaval and Dumouchel, 2001), and according to Yoon's experimental observations (Yoon et al., 2004), these large ones are usually found at the water-air boundary area. The velocity that one droplet may have at this area is usually very low because of the momentum exchange between fluid and air. Besides, the waterjet peening moves transversely when machining the target material. Impact pressure of the center liquid column is dominant, so that the impact from the fringe would be overwhelmed by the upcoming "central liquid column". Therefore in the present study, the contribution from the relative larger droplets is not considered.

The classification of velocity depends on its maximum velocity at a given standoff distance of waterjet. Taking Arola's experiment (Arola et al., 2001) as an example, for 280 MPa inlet pressure case, the maximum velocity at standoff distance 150 mm is 711 m/s, then 7 classes can be created from 100 to 700 m/s with an equal interval of 100 m/s. If the droplet impact velocity is lower than 100 m/s, it won't cause any plastic deformation on the target material Ti6Al4V no matter which size of droplet based on our preliminary simulation test.

10 classes of diameter times 7 classes of velocity yield 70 characteristic cases. The computational cost is acceptable. We developed a Python code

for batch processing, the total computational time from creating parts to the end of extracting data is around 6 hours (Intel Core i7-6700 CPU, 32 GB RAM, 8 cores).

2.2. Coupled Eulerian Lagrangian model

The CEL technique, available in Abaqus/Explicit (Abaqus, 2014) overcomes the difficulty that no single numerical method is applicable to the entire dynamic fluid-structure problem. In a traditional Lagrangian analysis the nodes are fixed within the material, and elements deform as the material deforms. This method is well-suited for the description of solid behavior. By contrast, in an Eulerian analysis, the nodes are fixed in space, and material flows through elements that do not deform. Such characteristics are particularly suitable for the large deformation problems of fluid/gas. Theory backgrounds and guidelines of CEL technique could be found in Abaqus documentation (Abaqus, 2014), as well as in Xie's thesis (Xie, 2014).

The basic assumptions for the CEL analysis are:

- The simplest case of a pure waterjet is that of a steady state waterjet with a full cone spray shape impinging perpendicular to the substrate.
- The target material is simplified as a semi-infinite deformable solid plate with a (clean) flat surface.
- Break-up and atomization of the waterjet are not considered at this stage since the present investigations are mainly confined to the roughening of substrate surface instead of the waterjets behavior.

A biocompatible titanium base alloy that is suitable for bone implant should have good workability and ductility(Oldani and Dominguez, 2012). The implant material should also have a high yield strength and fatigue strength to sustain cyclic loading. Ti6Al4V, a common implant metallic material, exhibits all those features. Therefore, an elastic-plastic nonlinear finite element analysis was performed using the commercial software Abaqus/Explicit, version 6.14 (Abaqus, 2014).

The one-fourth 3D model shown in Fig. 2 contains 1015625 EC3D8R (an 8-node linear Eulerian brick with reduced integration) and 116160 C3D8R (an 8-node linear hexahedral element with reduced integration) elements. The dimension of the target plate is length=width=$2.5D_d$, and height=$0.5D_d$. The Eulerian domain must be sufficiently big to capture all the potential

deformation behavior of droplet, whose dimension is $2.5D_d \times 2.5D_d \times 1.2D_d$. The boundary conditions for Eulerian and Lagrangian parts are shown in Fig. 3. One can use prescribed velocity or acceleration conditions on Eulerian nodes to control material flow. Vertical boundaries of the Lagrangian mesh are constrained as a symmetry boundary condition, and the bottom boundary against displacement in all directions. Material properties for water (Hamashima et al., 2004) and Ti6Al4V (Dorogoy and Rittel, 2009) are listed in Tab. 1.

One of the remarkable differences between Eulerian and Lagrangian approach in Abaqus/Explicit (Abaqus, 2014) is the way how to assign material property. Under Eulerian frame, the material is tracked as it flows through the mesh by computing its Eulerian Volume Fraction (EVF) within each element. By definition, if a material completely fills an element, its volume fraction is one; if no material is present in an element, its volume fraction is zero. Eulerian elements may simultaneously contain more than one material. If the sum of all material volume fractions in an element is less than one, the remainder of the element is automatically filled with 'void' material. The void material has neither mass nor strength.

The volume fraction tool available in Abaqus/Explicit (Abaqus, 2014) creates a discrete field by performing a Boolean comparison between an Eulerian part instance and a second part instance (the reference part instance, i.e., the droplet part) that intersects the Eulerian instance. The comparison determines where the two part instances overlap, then assigns each element in the Eulerian instance a volume fraction based on the percentage of the element that is also occupied by the reference instance. The volume fraction is specified as a decimal between zero and one. Thus this discrete field can be used to assign material instances to the Eulerian part instance.

2.3. Hybrid framework

Fig. 4 shows the framework of hybrid analysis procedures. In the present investigation, droplets are generated randomly, and their diameters and velocities follow Gaussian distribution because of its mathematical simplicity. Of course, the other well-known distributions which are mentioned earlier could be used as well, and they may reproduce experimental measurements more accurately, nevertheless, all distributions are applicable conditionally if the parameters (such as the standard deviation for the log-normal) are cautiously tuned and optimized to yield 'realistic' modeling.

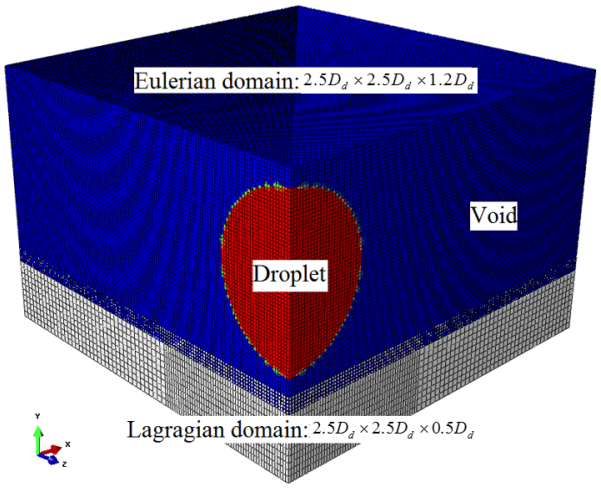

Figure 2: Mesh structure of 3D CEL model.

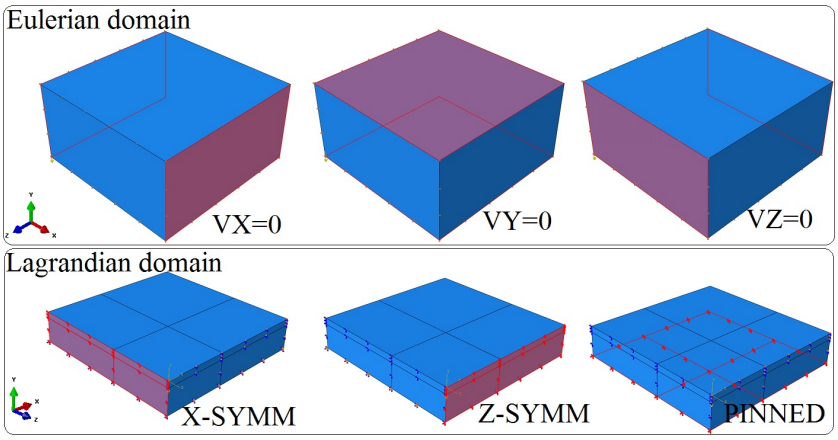

Figure 3: Boundary conditions defined in the CEL simulation.

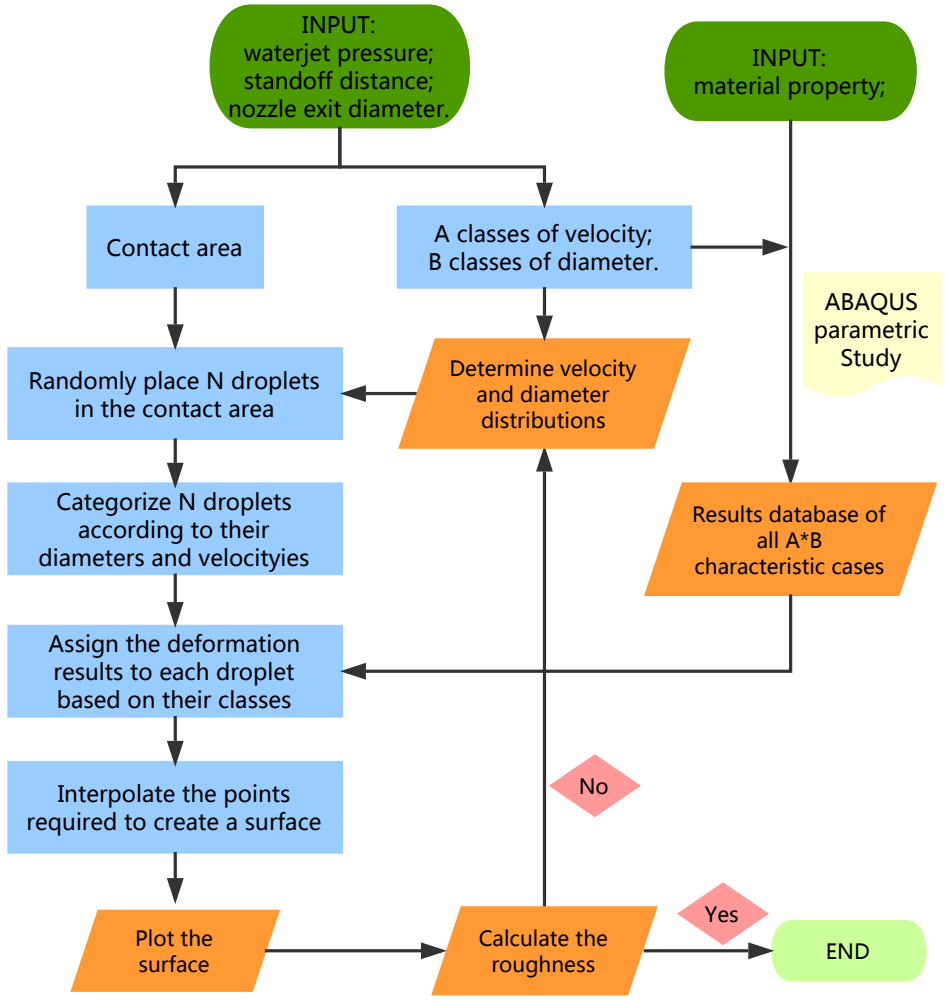

Figure 4: Schematic presentation of the calculation procedures along with the hybrid framework.

Table 1: The material properties of water and Ti6Al4V.

Material	Property	Value
Water	Density, ρ (Kg/m^3)	1×10^{-3}
	Viscosity, ν (Pa.s)	1×10^{-3}
	Shock velocity, C_0 (m/s)	1476
	Slope in U_s versus U_p, s	2
	Grüneison coefficient, Γ_0	1.65
Ti6Al4V	Density, ρ (Kg/m^3)	4.43×10^3
	Youngs Modulus, E(Pa)	1.14×10^{11}
	Poissons ratio, ν	0.342
	Yield stress, σ_y (Pa)	880×10^6

3. Simulation results

3.1. Single droplet

The deformation profiles and volume average pressure of droplet at different simulation time are shown in Fig. 5 and 6, respectively. Here, taking the case D_d=100 μm and v=700 m/s as an example. During the high pressure stage (before 36 ns), the water droplet behaves in a compressible manner (Field, 1999). This stage is maintained while the edge of the contact area moves faster than the shock velocity in the water. After that, the droplet spreads accompanying smaller droplets appeared at the periphery of the droplet, as Fig. 5(d) and (e) indicated. The pressure inside the droplet during this period decreases from the maximum 2.013 GPa at the contact periphery to about 250 MPa at the central area. In short, it follows this procedure: initial contact - compress - spread.

Due to the sudden deceleration of droplet and the consequently sharp rise of the impact pressure, the target material surface undergoes a severe plastic deformation at the initial contact stage, the Equivalent Plastic Strain (PEEQ) contours of target material displayed in Fig. 7 clearly show this phenomenon. The maximum plastic deformation is about 8.8% at the periphery of the contact area, where $r \approx 0.2D_d$. The PEEQ distribution barely changes after 36 ns, which means the water-hammer pressure at the initial stage of impact plays an absolute dominant role in the plastic deformation of the target material.

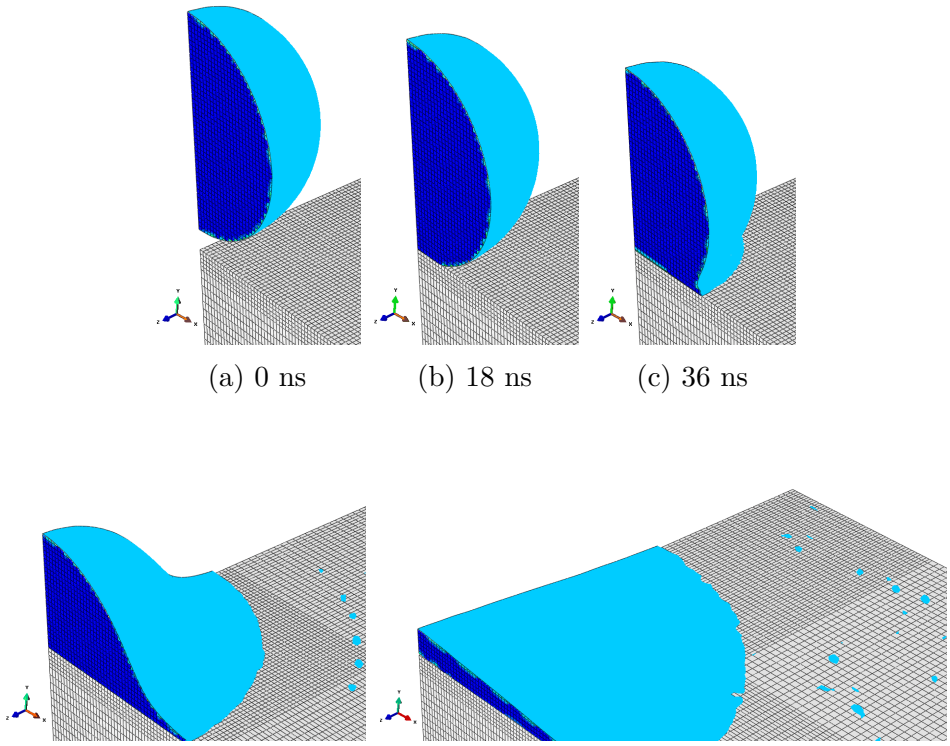

(a) 0 ns (b) 18 ns (c) 36 ns

(d) 84 ns (e) 228 ns

Figure 5: The deformation profiles of the droplet at different simulation time (D_d=100 μm, v=700 m/s).

The vertical displacement of target material shown in Fig. 8 clarifies the above fact from another aspect. Under high pressure impact, a crater is formed with a maximum depth at the center of the target material, and the data at that point are extracted and plotted in Fig. 8. After achieving the maximum indentation at the beginning, the droplet rebounds due to the release of elastic energy stored in the target material, which itself is oscillatory, as a result of the transient impact process. Eventually, displacement stabilizes, and the final displacements for all 70 characteristic cases are extracted for the next calculation (profile roughness). The data of these displacements are plotted in Fig. 9 by a 3D pattern. The trend is obvious, which the crater depth has a positive correlation with the impact velocity and diameter of droplet.

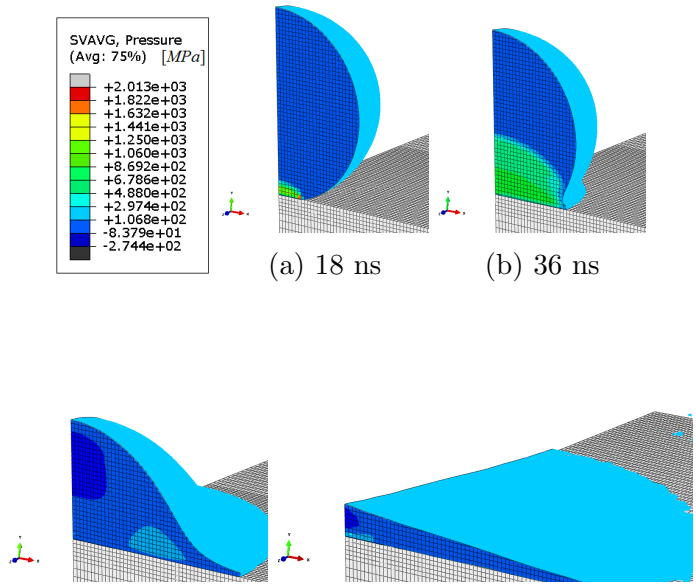

(a) 18 ns (b) 36 ns

(c) 84 ns (d) 228 ns

Figure 6: The contours of volume average pressure of droplet at different simulation time (D_d=100 μm, v=700 m/s).

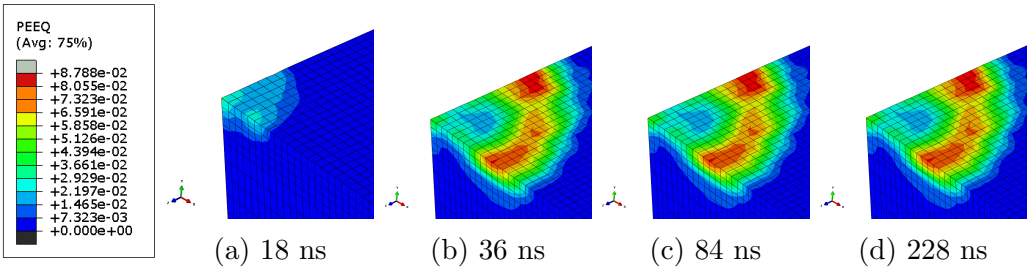

(a) 18 ns (b) 36 ns (c) 84 ns (d) 228 ns

Figure 7: The contours of equivalent plastic strain of target material at different simulation time (D_d=100 μm, v=700 m/s).

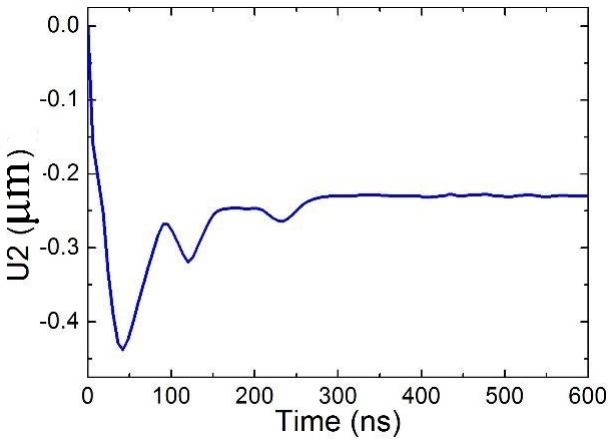

Figure 8: Time history of y-axis displacement ($U2$) at the center of the target material (D_d=100 μm, v=700 m/s).

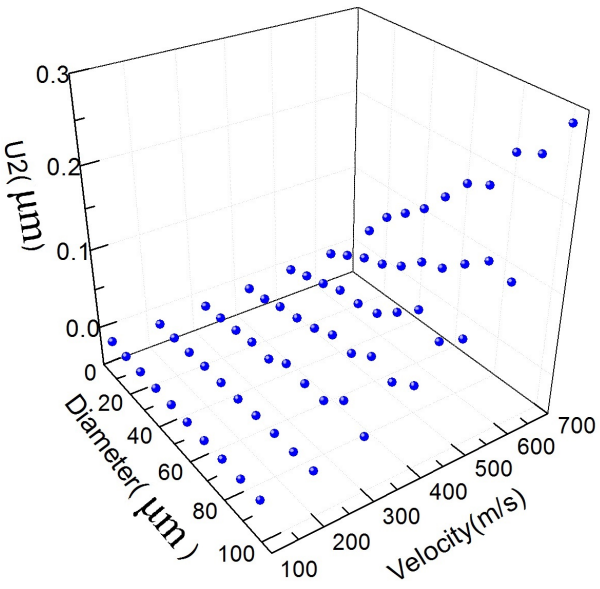

Figure 9: Y-axis displacement ($U2$) results of target surfaces of all characteristic cases.

3.2. Stochastic analysis

In the circular contact area, 1000,5000,10000 and 20000 droplets are placed randomly by using the 'unifrnd' function available in MATLAB (ver. R2016a) (MATLAB, 2016), and 4 images shown in Fig. 10 report their footprints. The following Fig. 11 displays their size distributions.

Based on our previous work (Xie and Rittel, 2017), the velocity distribution $v(x, y)$ of droplets can be written as:

$$v(x, y) = (1 - \frac{0.0003x}{D})v_0 exp(-2428.5\frac{y^2}{x^2}) \tag{6}$$

where x and y stand for the distance along the axial and radial direction, respectively; v_0 and D stand for the nozzle exit velocity and the nozzle exit diameter, respectively.

The velocity of each droplet is determined by Eq. 6. Clearly, more droplets bring to a higher coverage of the contact area. For 20000 droplets case, it almost fully filled with blue dots which is a symbol characterizing a single droplet. In these figures, the radius of blue dots, that seems equal to everyone, are not their 'real' radius. Actually, in the calculation, each blue dot has its own radius. One possible situation would be that the 10000 droplets have already covered the entire contact area with the overlap among droplets. Dai (Dai et al., 2004)presented similar images of 5/7.9 mm WC/Co balls for the analysis of shot peening, but he stopped at this conceptual step and didn't elaborate further. Fig 10, on the contrary, is our "starting point".

The roughness profiles shown in Fig. 13 are obtained from the center cross section where $Y = 0$. The sampling length in the direction of the x-axis used to identify the irregularities is about 6 mm, and the red dash line in the figure corresponds to the average height of measured roughness. Surface roughness parameters are calculated from the respective surface profiles and are listed in Tab. 2. The arithmetic average height R_a and quadrature average R_q have the same trend, which is the values increase initially with the number of droplets until 10000 droplets and approach a constant value after the impingements of 20000 droplets. Both R_a and R_q undergo three main stages: roughness increase, decrease, and final steady-state stage. Such a general trend as a function of a number of droplets can be understood qualitatively. At the initial stage, the R_a and R_q continuous to rise due to the newly-created craters on the original flat surface. Then peak regions would be impacted multiple times, and become blunt, resulting in a decline of arithmetic-mean roughness. Final stage may result in a dynamic equilibrium between generating new

Table 2: Calculated values of different roughness parameters.

Counts	$R_a(\mu m)$	$R_t(\mu m)$	$R_q(\mu m)$	$R_{sk}(\mu m)$	$R_{ku}(\mu m)$
1000	0.052	0.263	0.067	-1.203	3.742
5000	0.064	0.254	0.076	-0.907	2.612
10000	0.050	0.236	0.058	-0.713	2.323
20000	0.049	0.218	0.058	-0.633	2.221

crater (stage I) and reducing peak-valley (stage II). R_t and R_{ku} describe the sharpness of the roughness profile. As a result of stage II, the sharp ridges formed in the first stage vanish gradually. The surface topographies in Fig. 12 show an obvious sharpness evolution. The last roughness parameter R_{sk}, which is negative for all four cases. It is used to measure the symmetry of the profile regarding the mean line over the sampling length. Therefore, when the roughness enters into the steady-state, smaller absolute value of R_{sk} indicates less asymmetry of roughness profile.

4. Discussion

Given a system consisting of an extremely large number of droplets, it is difficult to predict the roughness by applying some physical laws to each individual droplet and all possible interactions between and among droplets. Even if it was possible to precisely predict the behavior of a single droplet, it would be prohibitively expensive to do so for the entire population of droplets. The FEM-Stochastic approach proposed here connects the single droplet to the many droplets system with the following two advantages. First is the ability to synthesize a surface roughness profile, and the ease of calculation of the relevant parameters of the roughness profile.

4.1. CEL analysis

Field et al. (Field and Lesser, 1977; Lesser and Field, 1983; Obara et al., 1995; Field, 1999) developed a theory for liquid impact on surfaces. For liquid impact on a rigid target, the contact pressure, frequently referred to as the "water-hammer" pressure, is:

$$P_c = \rho V C_1 \tag{7}$$

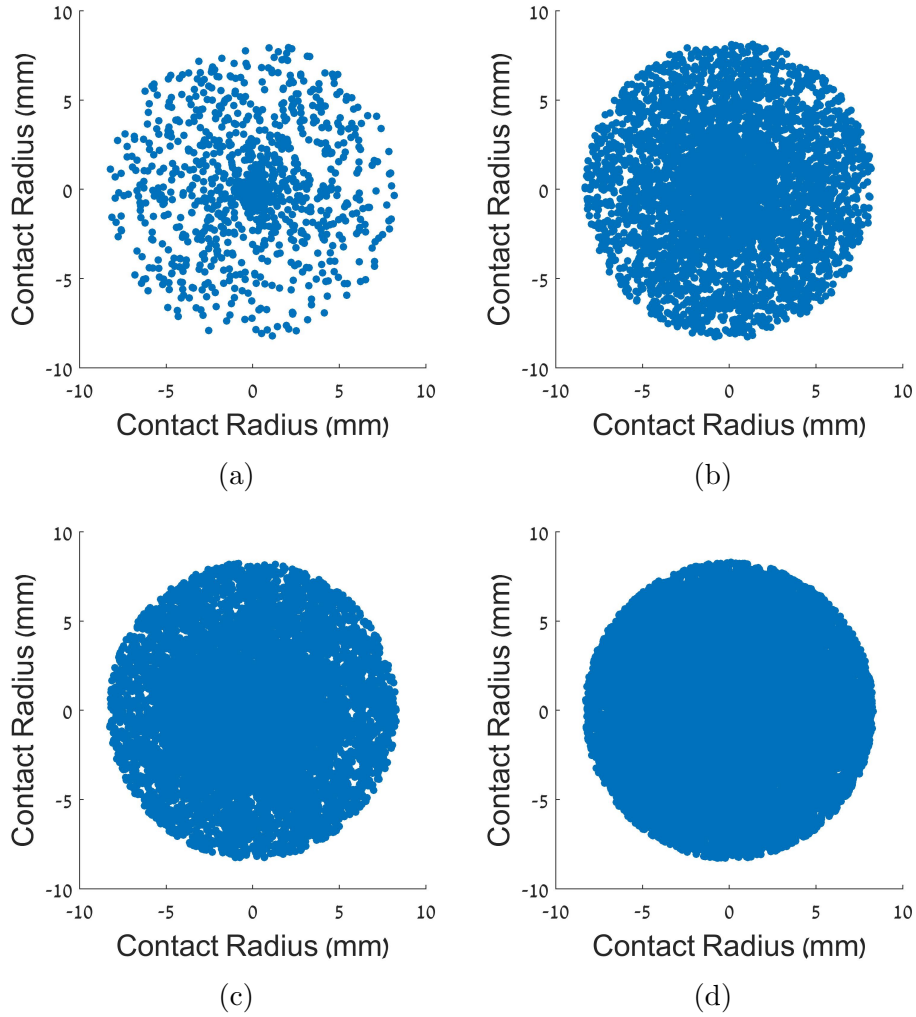

Figure 10: Footprints of artificial droplets. (a) 1000 droplets; (b) 5000 droplets; (c) 10000 droplets; (d) 20000 droplets.

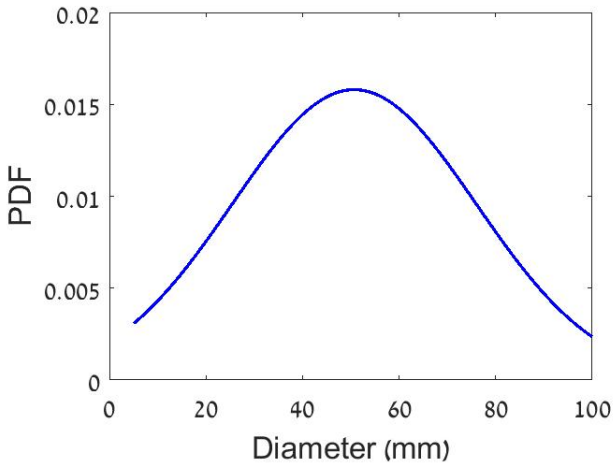

Figure 11: Size distribution used in the calculation. (PDF is the abbreviation of Probability Density Function.)

where ρ is the density of water, V is the impact velocity of waterjet and C_1 is the shock velocity of water.

The shock velocity of water C_1 can be determined from the relation:

$$C_1 = C_0 + kV \tag{8}$$

where C_0 is the acoustic velocity of water (around 1476 m/s), and k is a constant, close to 2 for water in the velocity range up to 1000 m/s.

The water-hammer pressure produced by a 100 μm water droplet with an impact velocity of 700 m/s, should be $P_c = 2.01$ GPa. From Fig. 6(a), it is clear that such high pressure correctly predicted by CEL simulation locates at the periphery of the contact area. After releasing high impact pressure, the pressure on the central axis falls to the much lower Bernoulli stagnation pressure $P_s = \rho V^2/2 = 245$ MPa. The simulation result displayed in Fig. 6(d) in a full agreement with the prediction of the stagnation pressure, that's validating the present CEL analysis.

4.2. Class width

In this study, the range between the minimum and the maximum diameter of the droplet is divided into 10 classes. The median diameter increases from the minimum 10 μm to the maximum 100 μm with an equal class width

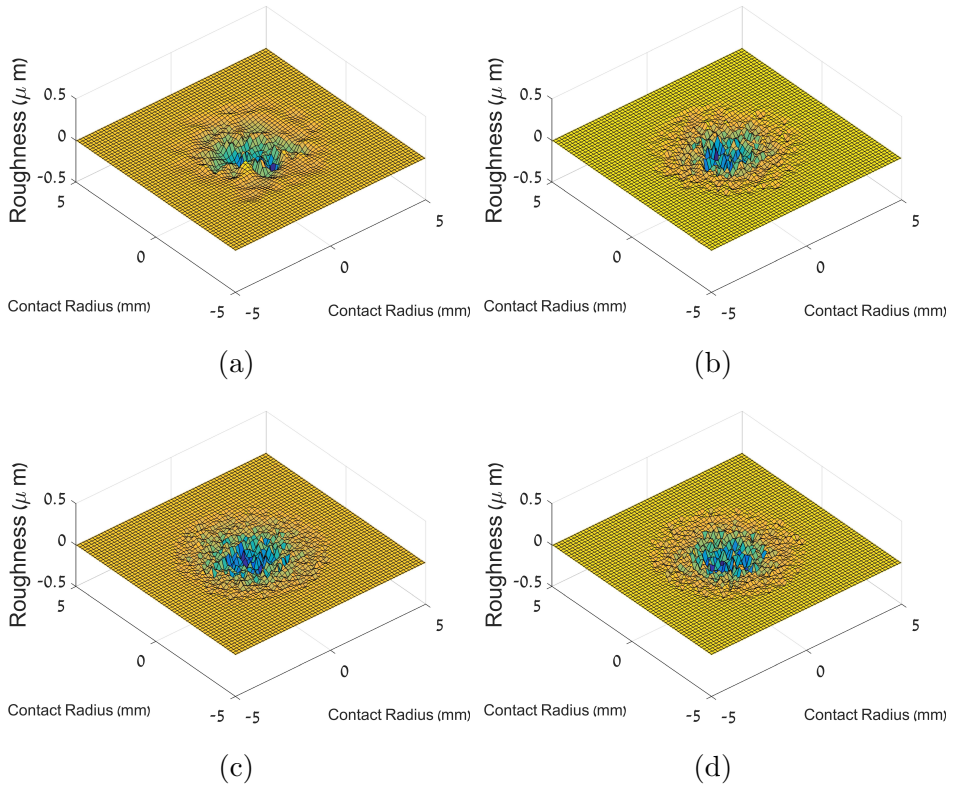

Figure 12: Deformed surfaces synthesized by the impingements of a different number of droplets. (a) 1000 droplets; (b) 5000 droplets; (c) 10000 droplets; (d) 20000 droplets.

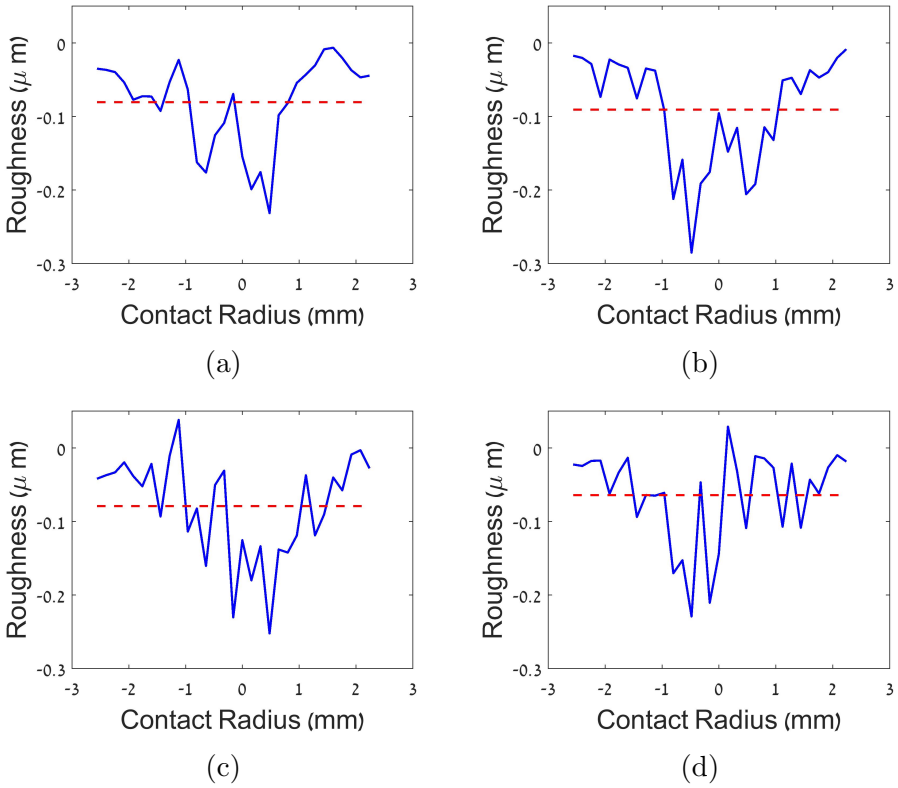

Figure 13: Roughness Profiles. (a) 1000 droplets; (b) 5000 droplets; (c) 10000 droplets; (d) 20000 droplets.

10 μm. Fig. 9 implies the influence of class width on the prediction of surface roughness. For lower impact velocity cases, such as 100 m/s, the class width has no influence on the maximum Y-axis displacement. Whether class width is larger or smaller, the simulation results of Y-axis displacement do not change significantly. For higher impact velocity cases, however, the class width contributes more on the accurate prediction of surface roughness. If the class width becomes smaller, e.g., 5 μm, we can describe more precisely the relationship between diameter and Y-axis displacement for a given impact velocity. Doing so, however, will sacrifice the computational efficiency because the number of characteristic single droplet cases multiplies.

As for the diameter, the prediction of surface roughness is affected by the class width of velocity as well. Through Fig. 9, the larger size of droplet is more sensitive to the change of impact velocity compared to the smaller droplet. If a droplet system contains many larger droplets, then a smaller interval of impact velocity, such as 50 m/s is able to alleviate the deviation caused by this simplification. Unavoidably, the number of characteristic single droplet cases rises.

Balancing the accuracy and efficiency of the calculations is a delicate task. What we did in this investigation is to keep a medium number of calculation jobs, which is 70. More flexible classification method can be used in the next step. For smaller droplets with lower impact velocity, still keep the current class width; for larger droplets with higher impact velocity, the class width can be properly smaller.

4.3. Spatial model of droplets

Taking R_a as an example, the experimental result for the case of 280 MPa is 2.4 μm (Arola et al., 2001), while our predicted value is only 0.05 μm. One possible reason for this underestimation lies in the spatial model of droplets. Those droplets perhaps follow a layer-by-layer impacting pattern, or the same area is impacted repeatedly by 100 droplets so to say. Several spatial models for multiple impacts, either stochastic or deterministic, have been proposed in the literature. Taro et al. (Taro et al., 2015) proposed a fully deterministic model assuming that impacts occur on a triangular mesh and at constant impact velocity, showing good agreement with experimental results. Rajesh (Rajesh and Ramesh Babu, 2006) proposed a finite element of multiple uniformly distributed impacts to predict residual stress instead of surface roughness. Hassani-Gangaraj et al. (Hassani-Gangaraj et al., 2015)

and Anwar et al. (Anwar et al., 2013) created finite element models containing a considerable number of solid particles. Their ideas could be a reference but should be used cautiously because they involve heavy computation load.

Performing an ergodic analysis for all the possible spatial organizations of multiple droplets is a difficult task. The interactions between and among droplets are still unclear. We do not know what kind of spatial model of droplets is more appropriate to represent the space position of myriads of droplets. Moreover, the deformation of target surface cannot increase all the way because of the work hardening of the target material, leading to some saturation. The size distribution of droplets, especially their spatial model, is crucial to the prediction of roughness that will be necessary in the future study of the kind showing here if a better agreement is sought between experimental and numerical results. Yet the present work indicates the important factors to be further studied and is aimed essentially at the presenting a new methodology.

5. Conclusions

We propose a new approach, combining finite element modeling and stochastic analysis, for the prediction of surface profile and roughness parameters.

The deformation pattern of single droplet follows this procedure: initial contact - compress - spread. Our CEL simulation results agree well the liquid impact theory, specifically the value and location of water-hammer pressure, and the stagnation impact pressure.

The water-hammer pressure at the initial stage of impact plays a dominant role in the plastic deformation of the target material. A higher impact velocity and a larger diameter of droplet both result in a deeper crater produced by single droplet impingement.

The arithmetic average height R_a and quadrature average R_q have the same trend, which is increase - decrease - stable three stages. The sharp ridges formed in the first stage vanish gradually leading to a decline of total roughness R_t and kurtosis parameter R_{ku}. Skewness parameter R_{sk} values of four cases are all negative, which means the roughness profiles have round peaks and sharp valleys. Along with the increasing of number of droplets, the roughness profile becomes more symmetrical as a result that the absolute value of R_{sk} becomes smaller.

Further effort must be invested in an accurate description of the spatial droplets distribution based on the experimental results that are not available today.

Acknowledgement

The work is supported in part at the Technion by a Technion-Guangdong Fellowship. Thanks for the enthusiastic help from all the colleagues of Dynamic Fracture Laboratory of Technion Israel Institute of Technology.

References

Abaqus, V., 2014. 6.14 documentation. Dassault Systemes Simulia Corporation.

Anwar, S., Axinte, D., Becker, A., 2013. Finite element modelling of overlapping abrasive waterjet milled footprints. Wear 303 (1), 426–436.

Arola, D., McCain, M., Kunaporn, S., Ramulu, M., 2001. Waterjet and abrasive waterjet surface treatment of titanium: a comparison of surface texture and residual stress. Wear 249 (10), 943–950.

Asadollahzadeh, M., Torkaman, R., Torab-Mostaedi, M., Safdari, J., 2017a. A comparison between drop size distributions derived from the probability distribution functions and maximum entropy principle. case study; pilot plant scheibel extraction column. Chemical Engineering Research and Design 117, 648–658.

Asadollahzadeh, M., Torkaman, R., Torab-Mostaedi, M., Safdari, J., 2017b. Using maximum entropy, gamma, inverse gaussian and weibull approach for prediction of drop size distribution in a liquid–liquid extraction column. Chemical Engineering Research and Design 117, 637–647.

Azzopardi, B. J., 2011. Sauter mean diameter. Thermopedia,[Online]. Available: http://www. thermopedia. com/content/1108/.[Accessed 01 03 2013].

Babinsky, E., Sojka, P., 2002. Modeling drop size distributions. Progress in energy and combustion science 28 (4), 303–329.

Boyaval, S., Dumouchel, C., 2001. Investigation on the drop size distribution of spraysproduced by a high-pressure swirl injector. measurementsand application of the maximum entropy formalism. Particle & Particle Systems Characterization 18 (1), 33–49.

Dai, K., Villegas, J., Stone, Z., Shaw, L., 2004. Finite element modeling of the surface roughness of 5052 al alloy subjected to a surface severe plastic deformation process. Acta Materialia 52 (20), 5771–5782.

Dorogoy, A., Rittel, D., 2009. Determination of the johnson–cook material parameters using the scs specimen. Experimental mechanics 49 (6), 881.

Dumouchel, C., 2009. The maximum entropy formalism and the prediction of liquid spray drop-size distribution. Entropy 11 (4), 713–747.

Field, J., 1999. Elsi conference: invited lecture: liquid impact: theory, experiment, applications. Wear 233, 1–12.

Field, J., Lesser, M., 1977. On the mechanics of high speed liquid jets. In: Proceedings of the Royal Society of London A: Mathematical, Physical and Engineering Sciences. Vol. 357. The Royal Society, pp. 143–162.

Hamashima, H., Kato, Y., Itoh, S., Furnish, M. D., Gupta, Y. M., Forbes, J. W., 2004. Determination of jwl parameters for non-ideal explosive. In: AIP Conference Proceedings. Vol. 706. AIP, pp. 331–334.

Hassani-Gangaraj, S., Cho, K., Voigt, H.-J., Guagliano, M., Schuh, C., 2015. Experimental assessment and simulation of surface nanocrystallization by severe shot peening. Acta Materialia 97, 105–115.

Hsu, C.-Y., Liang, C.-C., Teng, T.-L., Nguyen, A.-T., 2013. A numerical study on high-speed water jet impact. Ocean Engineering 72, 98–106.

Lesser, M., Field, J., 1983. The impact of compressible liquids. Annual review of fluid mechanics 15 (1), 97–122.

Li, X., Chin, L., Tankin, R., Jackson, T., Stutrud, J., Switzer, G., 1991. Comparison between experiments and predictions based on maximum entropy for sprays from a pressure atomizer. Combustion and flame 86 (1-2), 73–89.

Li, X., Tankin, R. S., 1992. On the prediction of droplet size and velocity distributions in sprays through maximum entropy principle. Particle & particle systems characterization 9 (1-4), 195–201.

Li, X., Tankin, R. S., Renksizbulut, M., 1990. Calculated characteristics of droplet size and velocity distributions in liquid sprays. Particle & particle systems characterization 7 (1-4), 54–59.

Ma, L., Bao, R.-h., Guo, Y.-m., 2008. Waterjet penetration simulation by hybrid code of sph and fea. International Journal of Impact Engineering 35 (9), 1035–1042.

Mabrouki, T., Raissi, K., Cornier, A., 2000. Numerical simulation and experimental study of the interaction between a pure high-velocity waterjet and targets: contribution to investigate the decoating process. Wear 239 (2), 260–273.

Maniadaki, K., Kestis, T., Bilalis, N., Antoniadis, A., 2007. A finite element-based model for pure waterjet process simulation. The International Journal of Advanced Manufacturing Technology 31 (9), 933–940.

MATLAB, 2016. version 9.0.0 (R2016a). The MathWorks Inc., Natick, Massachusetts.

Obara, T., Bourne, N., Field, J., 1995. Liquid-jet impact on liquid and solid surfaces. Wear 186, 388–394.

Oldani, C., Dominguez, A., 2012. Titanium as a biomaterial for implants. In: Recent Advances in Arthroplasty. InTech.

Rajesh, N., Ramesh Babu, N., 2006. Multidroplet impact model for prediction of residual stresses in water jet peening of materials. Materials and manufacturing processes 21 (4), 399–409.

Rioboo, R., Tropea, C., Marengo, M., 2001. Outcomes from a drop impact on solid surfaces. Atomization and Sprays 11 (2).

Sellens, R., Brzustowski, T., 1986. A simplified prediction of droplet velocity distributions in a spray. Combustion and Flame 65 (3), 273–279.

Sellens, R. W., 1989. Prediction of the drop size and velocity distribution in a spray, based on the maximum entropy formalism. Particle & Particle Systems Characterization 6 (1-4), 17–27.

Sellens, R. W., 2016. Drop size and velocity distributions in sprays, a new approach based on the maximum entropy formalism.

Shinjo, J., Umemura, A., 2010. Simulation of liquid jet primary breakup: Dynamics of ligament and droplet formation. International Journal of Multiphase Flow 36 (7), 513–532.

Taro, M., Chaise, T., Nélias, D., 2015. A methodology to predict the roughness of shot peened surfaces. Journal of Materials Processing Technology 217, 65–76.

Wenjun, G., Jianming, W., Na, G., 2011. Numerical simulation for abrasive water jet machining based on ale algorithm. The International Journal of Advanced Manufacturing Technology 53 (1), 247–253.

Worthington, A., 1876. On the forms assumed by drops of liquids falling vertically on a horizontal plate. Proceedings of the royal society of London 25 (171-178), 261–272.

Xie, J., 5 2014. Simulation of cold spray particle deposition process. Ph.D. thesis, INSA De Lyon.

Xie, J., Nélias, D., Walter-Le Berre, H., Ogawa, K., Ichikawa, Y., 2015. Simulation of the cold spray particle deposition process. Journal of Tribology 137 (4), 041101.

Xie, J., Rittel, D., 2017. A two-dimensional model for metallic surface roughness resulting from pure waterjet peening. International Journal of Engineering Science 120, 189 – 198.

Yarin, A., 2006. Drop impact dynamics: splashing, spreading, receding, bouncing. Annu. Rev. Fluid Mech. 38, 159–192.

Yoon, S., Hewson, J., DesJardin, P., Glaze, D., Black, A., Skaggs, R., 2004. Numerical modeling and experimental measurements of a high speed solid-cone water spray for use in fire suppression applications. International Journal of Multiphase Flow 30 (11), 1369–1388.